



On a Solar Blowout Jet: Driving Mechanism and the Formation of Cool and Hot Components

Yuandeng Shen^{1,2,3,4} , Ying D. Liu^{2,5} , Jiangtao Su^{3,5}, Zhining Qu⁶ , and Zhanjun Tian^{1,5} 

¹Yunnan Observatories, Chinese Academy of Sciences, Kunming, 650216, China; ydshen@ynao.ac.cn

²State Key Laboratory of Space Weather, Chinese Academy of Sciences, Beijing 100190, China

³Key Laboratory of Solar Activity, National Astronomical Observatories of Chinese Academy of Science, Beijing 100012, China

⁴Center for Astronomical Mega-Science, Chinese Academy of Sciences, Beijing, 100012, China

⁵University of Chinese Academy of Sciences, Beijing 100049, China

⁶School of Physics and Electronic Engineering, Sichuan University of Science & Engineering, Zigong 643000, China

Received 2017 June 5; revised 2017 November 6; accepted 2017 November 6; published 2017 December 13

Abstract

We present observations of a blowout jet that experienced two distinct ejection stages. The first stage started from the emergence of a small positive magnetic polarity, which was cancelled by the nearby negative magnetic field and caused the rising of a mini-filament and its confining loops. This further resulted in a small jet due to the magnetic reconnection between the rising confining loops and the overlying open field. The second ejection stage was mainly due to successive removal of the confining field by reconnection: the filament erupted, and the erupting cool filament material directly combined with the hot jet that originated from the reconnection region and therefore formed the cool and hot components of the blowout jet. During the two ejection stages, cool $H\alpha$ jets are also observed cospatial with their coronal counterparts, but their appearance times are earlier by a few minutes than those of the hot coronal jets. The hot coronal jets are therefore possibly caused by the heating of the cool $H\alpha$ jets or the rising of the reconnection height from the chromosphere to the corona. The scenario that magnetic reconnection occurred between the confining loops and the overlying open loops is supported by many observational facts, including the bright patches on both sides of the mini-filament, hot plasma blobs along the jet body, and periodic metric radio type III bursts at the very beginnings of the two stages. The evolution and characteristics of these features show the detailed nonlinear process in magnetic reconnection.

Key words: Sun: activity – Sun: filaments – prominences – Sun: flares – Sun: magnetic fields

Supporting material: animation

1. Introduction

Solar jets are collimated hot plasma flows along vertical or oblique magnetic field lines. They are ubiquitous in the solar atmosphere from the photosphere to the outer corona. Although researches of solar jets have a long history, many physical questions about their detailed magnetic structure and formation mechanism are still unclear. Previous observational studies have suggested that most solar jets are formed by magnetic reconnection between emerging bipoles and their ambient open magnetic field lines (e.g., Shibata et al. 1994b; Liu & Kurokawa 2004; Shen et al. 2011; Li et al. 2012; Chen et al. 2012; Li et al. 2015; Lim et al. 2016). However, magnetic flux cancellation is sometimes also important to the generation of solar jets (e.g., Shen et al. 2012; Yang et al. 2012a, 2016; Adams et al. 2014; Li et al. 2016; Panesar et al. 2016; Joshi et al. 2017). Moreover, Shen et al. (2014) reported that large-scale coronal waves can also lead to coronal jet by disturbing the coronal magnetic field at the boundary of coronal holes. Solar jet or jet-like phenomena are always associated with micro-flares that transfer magnetic energy to heat and kinetic energy. Since the occurrence rate of jets or jet-like activities is very high in the solar atmosphere, some solar physicists have proposed that solar jets might be a candidate source for heating the coronal plasma and accelerating the fast solar wind (Innes et al. 1997; Shibata et al. 2007; Tian et al. 2014). In addition, observational studies also indicated that some jet activities can directly or indirectly result in large-scale magnetic reconfigurations such as coronal mass ejections (CMEs; Wang et al. 1998;

Liu et al. 2005; Liu 2008; Shen et al. 2012; Liu et al. 2015), filament or loop eruptions (e.g., Jiang et al. 2008; Wang et al. 2016; Zheng et al. 2016), and coronal waves (Zheng et al. 2012, 2013; Su et al. 2015). Therefore, investigating the driving and evolution mechanisms of solar jets is very important in solar physics.

Currently, there are three main classification methods for solar jets. First, solar jets can be divided into surges ($H\alpha$), extreme ultraviolet (EUV) jets (EUV), and X-ray jets (X-ray) according to different observing wavelengths. Second, according to their different driving mechanisms and morphology, solar jets are classified into the so-called “anemone jet” and the “two-sided loop jet” (Shibata et al. 1994a; Yokoyama & Shibata 1995; Jiang et al. 2013; Tian et al. 2017). They are thought to be formed by magnetic reconnection between emerging bipoles and the ambient oblique or horizontal magnetic field lines, respectively. It should be pointed out that the two-sided loop jets can also be produced via the so-called tether-cutting reconnection (Moore et al. 2001; Chen et al. 2014, 2016; Xue et al. 2017) between two adjacent filamentary threads (Yang et al. 2016; Tian et al. 2017). Third, Moore et al. (2010) performed a statistical analysis and claimed that there is a dichotomy of coronal jets according to their different eruption characteristics. The authors named them “standard jet” and “blowout jet”. The former is similar to the standard reconnection picture for coronal jets, while the latter is often associated with erupting loops or twisted small filaments in the jet-base. So far there are many studies based on high-resolution observations which have confirmed the finding of blowout jets

(e.g., Shen et al. 2012; Yang et al. 2012b; Pucci et al. 2013; Kayshap et al. 2013; Adams et al. 2014; Young & Muglach 2014; Hong et al. 2013, 2016, 2017; Li et al. 2015; Sterling et al. 2016; Lim et al. 2016; Zhang & Zhang 2017; Zhu et al. 2017), and a few observational studies further investigated the relationship between blowout jets and CMEs (Hong et al. 2011; Shen et al. 2012). Especially, Shen et al. (2012) reported that a single blowout jet can lead to a jet-like and a simultaneous bubble-like CME. They proposed that the jet-like CME results from the outward-moving hot plasma that is produced in the magnetic reconnection between the emerging bipole and the ambient open field lines, while the bubble-like CME is caused by the eruption of the mini-filament that is confined by the emerging bipole. Furthermore, numerical simulation studies of coronal blowout jets are also preformed by many authors (e.g., Pariat et al. 2009; He et al. 2010; Pariat et al. 2010; Archontis & Hood 2013; Ni et al. 2015; Pariat et al. 2015, 2016; Wyper et al. 2016; Wyper & DeVore 2016; Wyper et al. 2017; Szente et al. 2017). Here, we would like to point out that before the conception of the blowout jet was first proposed, a few observations had indicated that some jets or surges are tightly related to mini-filament or loop eruptions (Chen et al. 2009; Nisticò et al. 2009). Very recently, Hong et al. (2014) observed many jet-like mini-filament eruptions from coronal bright points. Sterling et al. (2015) further proposed that almost all coronal jets originate from mini-filament eruptions, and they also suggested that standard and blowout jets are fundamentally the same phenomenon. If the eruption of a filament fails or succeeds to escape the confining closed-field jet-base, the consequence is that the eruption forms a standard or blowout jet, respectively. These studies together suggest that filament eruptions are deeply involved in jet activities, and different solar eruption phenomena might obey a universal eruption model (Shen et al. 2012; Wyper et al. 2017).

In recent years, many new characteristics of solar jets have been discovered by using high temporal and high spatial resolution observations. For example, Shen et al. (2011) presented an unwinding polar coronal jet that exhibits intriguing bright helical fine structure that twists the jet body, and they described three distinct expansion phases in the lateral direction. The unwinding motion of the coronal jet is thought to be caused by the release of magnetic twist stored in the emerging bipole via magnetic reconnection between the bipole and the ambient open field lines. The measured released magnetic twists during the ejection is about 1.17–2.55 turns, which is comparable to typical active region filaments (Yan et al. 2014, 2015). In addition, the three distinct expansion phases are possibly associated with the different stages in the nonlinear magnetic reconnection process, and this hypothesis has recently been confirmed by Chen et al. (2017). So far, many studies have also reported rotational motion of coronal jets (e.g., Zhang et al. 2000; Liu et al. 2009; Curdt & Tian 2011; Curdt et al. 2012; Hong et al. 2013; Schmieder et al. 2013; Lee et al. 2013; Zhang & Ji 2014a; Filippov et al. 2015; Moore et al. 2015; Li et al. 2017a, 2017b), and Chen et al. (2012) even estimated the magnetic field strength of a rotational jet to be 15 to 3 Gauss from the jet-base to the top. To the best of our knowledge, rotational motion is not a common characteristic for all coronal jets, but it is indeed frequently observed in coronal blowout jets. The reason might be that blowout jets are often associated with twisted filament

eruptions that transfer magnetic twist to the open fields and therefore drive the jet rotation (Shibata & Uchida 1986; Canfield et al. 1996). Sometimes, coronal jets can occur repeatedly at the same position; they are often associated with successive magnetic flux emergence and cancellation processes at the jet source region (Jiang et al. 2007; Yang et al. 2011; Jiang et al. 2013; Chen et al. 2008; Chifor et al. 2008; Li et al. 2015), as well as with moving magnetic features (e.g., Brooks et al. 2007; Chen et al. 2015). Using a magnetic extrapolation method and analyzing the change of current in the jet source region, Guo et al. (2013) proposed that periodic magnetic reconnection can result in recurrent coronal jets as well. In addition, the oscillation of coronal jets is thought to be evidence of propagating Alfvén waves (Nishizuka et al. 2008; Liu et al. 2009; Lee et al. 2013, 2015).

An important characteristic of solar jets is that some coronal jets consist of both cool and hot plasma flows (e.g., Mulay et al. 2017), and the cool component is often delayed with respect to the hot component. Canfield et al. (1996) reported that chromospheric $H\alpha$ surges are spatially adjacent to the corresponding coronal X-ray jets. Jiang et al. (2007) also observed a similar spatial relationship between surges and coronal jets, and they further reported that the start of $H\alpha$ surges is slightly delayed to the beginning of the corresponding coronal jets. Previous studies indicated that the delay-time interval ranges from 2 to 15 minutes, and most authors explained this phenomenon as the cooling of the earlier and hotter coronal jet material (e.g., Schmieder et al. 1994; Alexander & Fletcher 1999; Jiang et al. 2007). However, there are still a few other interpretations for the formation and the delay of the cool component. For example, Nishizuka et al. (2008) reproduced both cool and hot components in their simulation, and they interpreted the delay of the jet's cool component as resulting from the different Alfvén velocities in the cool (high-density) and hot (low-density) plasmas rather than the cooling effect, since they found that the delay time is much shorter than the cooling time of the hot plasma flow. Yokoyama & Shibata (1995) also generated hot and cool plasma components in their simulation, and they explained that the cool component of coronal jets is formed by chromospheric cool plasmas that are carried up with expanding loops and are accelerated by the tension force of disconnected field lines. Chae et al. (1999) found that the coronal jets are identified with bright jet-like features in the $H\alpha$ line center, and they claimed that their observation confirms the simulation result of Yokoyama & Shibata (1995). In addition, Lee et al. (2013) also proposed that the cool component of the jet is caused by reconnection of emerging flux in the transition region or upper chromosphere. Recently, Shen et al. (2012) observed the appearance of both hot and cool components in a typical coronal blowout jet with stereoscopic high-resolution observations. They observed similar characteristics as were reported in previous articles, such as the spatial relationship and the delay appearance of the cool component. They clearly showed that the cool component of the coronal jet is actually formed by the erupting small filament that is confined by the jet-base, while the hot component resulted from the heated plasma during the reconnection between the jet-base and the ambient open magnetic field lines. So far, the formation mechanism of the cool component of coronal jets is still an open question, and more details about coronal jets can be found in a recent review article (Raouafi et al. 2016).

In this paper, we present an observational study of the formation of cool and hot plasma structures and plasma blobs in a miniature coronal blowout jet, using the high temporal and high spatial resolution data provided by the New Vacuum Solar Telescope (NVST; Liu et al. 2014; Xiang et al. 2016) and the Atmospheric Imaging Assembly (AIA; Lemen et al. 2012) on board the *Solar Dynamics Observatory* (SDO; Pesnell et al. 2012). The presented event occurred on April 16, 2014 at the southern periphery region of NOAA active region 12035. We find that the cool component of the coronal jet is directly formed by the eruption of a mini-filament at the jet-base. In addition, successive hot plasma blobs are observed moving along the jet body, and metric type III radio burst are also detected during the initiation and violent ejection phases of the jet. These results provide evidence supporting the scenario that the blowout jet was driven by the magnetic reconnection process. The instruments and data set we used are briefly introduced in Section 2. The analysis results are described in Section 3. Conclusions and discussions are highlighted in the last section.

2. Observations

The NVST is a new one-meter solar telescope operated by the Yunnan Observatories. It is located at the northeast side of Fuxian Lake, Yunnan, China. The primary goals of the NVST are high-resolution imaging, spectral observation, and measurements of the solar magnetic field. Currently, the NVST mainly observes the photosphere and chromosphere using TiO-band, G-band, and $H\alpha$ lines. We only use the $H\alpha$ line-center observations in the present paper. These observations have a cadence of 12 s and a spatial resolution of $0''.3$. Owing to the influence of the Earth's turbulent atmosphere, the raw solar images taken by the NVST are reconstructed using high-resolution imaging algorithms (Liu et al. 2014). The AIA on board the SDO images the full-disk Sun using seven EUV and three UV wavelengths. It takes EUV (UV) images every 12 (24) seconds with a pixel size of $0''.6$. The line-of-sight (LOS) magnetograms taken by the Helioseismic and Magnetic Imager (HMI; Schou et al. 2012) on board SDO are also used to analyze the magnetic field topology, which has a cadence of 45 seconds and a measurement precision of 10 Gauss. All images used in this paper are differentially rotated to the reference time of 07:30:00 UT. In addition, metric radio observations recorded by the metric spectrometer of the Yunnan Observatories (YNAO; Gao et al. 2014a) are also used in the present paper to diagnose the detailed magnetic reconnection processes, which work in the frequency range of 70–700 MHz with a spectral resolution of 200 kHz, a time cadence of 90 ms, and a high sensitivity lower than 1 sfu.

3. Results

The presented event occurred on 2014 April 16 at the southern periphery region of NOAA active region AR12035, which was close to the solar disk center. The ejection of the blowout jet was associated with the eruption of a mini-filament that had a projection length of 13 Mm. According to previous statistical results, the length of the mini-filament is much shorter than the average projection length of mini-filaments (19 Mm; Wang et al. 2000).

An overview of the eruption source region before the start of the jet is shown in Figure 1. It can be seen that the source region

is located at the southern periphery of the leading sunspot of active region AR12035, which is close to the disk center of the Sun. The magnetic field of the source region is a mixed-polarity region that is composed of many small positive and negative polarities (see Figure 1(b)). A mini-filament can be identified from the $H\alpha$ image in the source region, and the outline contour sketch is overlaid on different wavelength images (see the white dotted contour in Figures 1(b)–(f)). At the same time, the contours of the HMI LOS magnetic field are also overlaid on the EUV observations to show the position relation between the filament and the surrounding magnetic field. From Figure 1, the filament can be clearly identified in the NVST $H\alpha$ line-center image, but it is hard to find the counterpart in the EUV images. It should be noted that the filament cannot be observed in the AIA 171 Å image before the ejection (Figure 1(d)), since it was covered by a bunch of coronal loops that were rooted in the leading sunspot of NOAA active region AR12035.

The ejection of the blowout jet underwent two distinct ejection stages. The first ejection stage is shown in Figure 2 with the NVST $H\alpha$ line center (10^4 K), AIA 171 (6.3×10^5 K), and 335 Å (2.5×10^6 K) images. The top row shows the NVST $H\alpha$ line-center images overlaid with the outline contour sketch of the mini-filament in each panel (white dotted contour). Before the ejection, one can see that there is a bunch of dark filamentary thread (north-south direction) across the western end of the filament (see Figures 2(a) and (b)). At about 07:11:43 UT, the dark filamentary thread started to move east. About 8 minutes later, a pair of brightening patches appeared on either side of the filament at about 07:19:23 UT (see the two black arrows in Figure 2(c)). In the meantime, a small dark jet is observed in $H\alpha$ observations, and it showed an eastward whip-like motion during the eruption (see the white arrow in Figure 2(c)). About one minute later, the pair of brightening patches and the body of the jet both became brighter than before (see the arrows in Figure 2(d)). It is hard to distinguish the ejecting $H\alpha$ jet from a single statical image, but it is clear in the online animation made from NVST $H\alpha$ time sequence of images.

In the AIA 171 and 335 Å observations, a small loop-like bright structure is observed at the crossing position of the filamentary thread and the mini-filament during the first ejection stage. It is interesting that this loop-like bright feature exactly connects the pair of brightening patches observed in the $H\alpha$ images (see the blue curve in Figure 2(d)). This suggests that the bright loop-like structure and the pair of brightening patches could be regarded as the manifestations of the magnetic reconnection between the filamentary thread and the underneath closed loops that prevent the mini-filament from erupting. A few minutes after the appearance of the bright loop-like feature, a collimated bright coronal jet is observed along the path of the $H\alpha$ filamentary thread. The outline contour sketch of the coronal jet detected from the AIA 171 Å image at 07:21:11 UT is overlaid on the $H\alpha$ image at 07:20:36 UT (see Figure 2(d)), and the result shows that the trajectory of the $H\alpha$ jet and the bright coronal jet are the same. In addition, it is also found that the beginning of the $H\alpha$ jet precedes the appearance of its coronal counterpart by about 2 minutes, which is inconsistent with previous observations that the cool component of solar jets delays the hot component by a few minutes (e.g., Schmieder et al. 1994; Alexander & Fletcher 1999; Jiang et al. 2007). However, the spatial relationship between the two jet components is in agreement with Chae et al. (1999). It

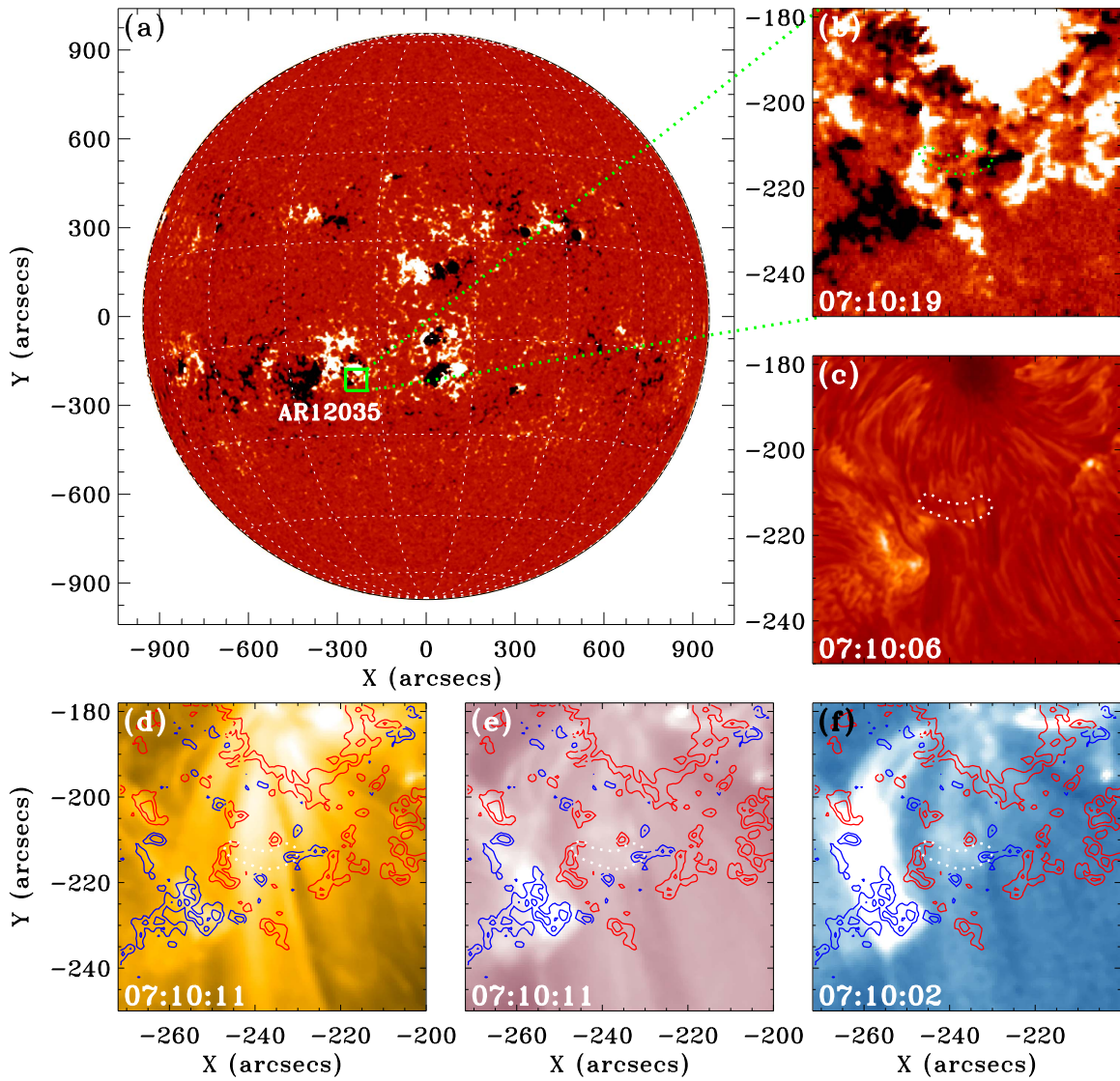


Figure 1. Overview of the event before the eruption. Panel (a): full-disk HMI LOS magnetogram, in which the white and black patches represent the positive and negative magnetic polarities, respectively. The green box shows the eruption source region, the details of which in other wavelengths are shown in the other panels. Panels (b) and (c): close view of the HMI LOS magnetogram and NVST H α -center images overlaid with the outline contour sketch of the mini-filament. Panels (d), (e), and (f): AIA 171, 211, and 335 images overlaid with the contours of the HMI LOS magnetic fields and the outline contour sketch of the mini-filament, in which the magnetic field contour levels are ± 50 , ± 100 , and ± 200 ; red and blue show positive and negative magnetic polarities.

should be emphasized that Figure 2 only shows some key snapshots of the ejection process. For a detailed evolution process of the jet, one can see the associated animation available in the online journal.

Following the end of the first ejection stage, the blowout jet started a more violent ejection stage that showed interesting cool and hot plasma flows adjacent to each other and bright plasma blobs along the jet axis. At about the start of the second ejection stage, a pair of H α brightening patches appeared on either side of the filament, as in the first ejection stage (see the two arrows in Figure 3(b)), then a relative larger H α jet formed and was ejected to the south (see the bright long arrows in Figures 3(c) and (d)). In the meantime, the H α jet showed an eastward whip-like motion. This result is in agreement with the scenario that the H α jet is caused by the eruption of the mini-filament. In AIA 171 and 335 \AA EUV observations, a pair of bright patches and a bright thin coronal jet are observed at the jet-base and along the path of the H α jet, respectively (see panels (f) and (j) in Figure 3), and the appearance of the coronal

jet delayed the H α jet for a few minutes. The outline contour sketch of the EUV jet determined from the AIA 171 \AA image at 07:39:23 UT is overlaid on the H α image at 07:40:35 UT, and the result indicates that the H α jet is also cospatial with its coronal counterpart, in agreement with the first ejection stage. Around 07:40:50 UT, the erupting cool filament material merged with the previously existing bright hot jet and thus formed the cool (dark) and hot (bright) components of the jet (see the black and white arrow in Figure 3(i)). The observational results indicate that the cool component of the jet is directly formed by the erupting filament. This is consistent with the results reported in Shen et al. (2012), but is inconsistent with previous studies, in which the cool components of jets are thought to be formed by the cooling of the hot component or other mechanisms (e.g., Schmieder et al. 1994; Alexander & Fletcher 1999; Jiang et al. 2007; Nishizuka et al. 2008; Yokoyama & Shibata 1995; Lee et al. 2013). An interesting phenomenon of the jet during the second ejection stage is the formation of many bright plasma

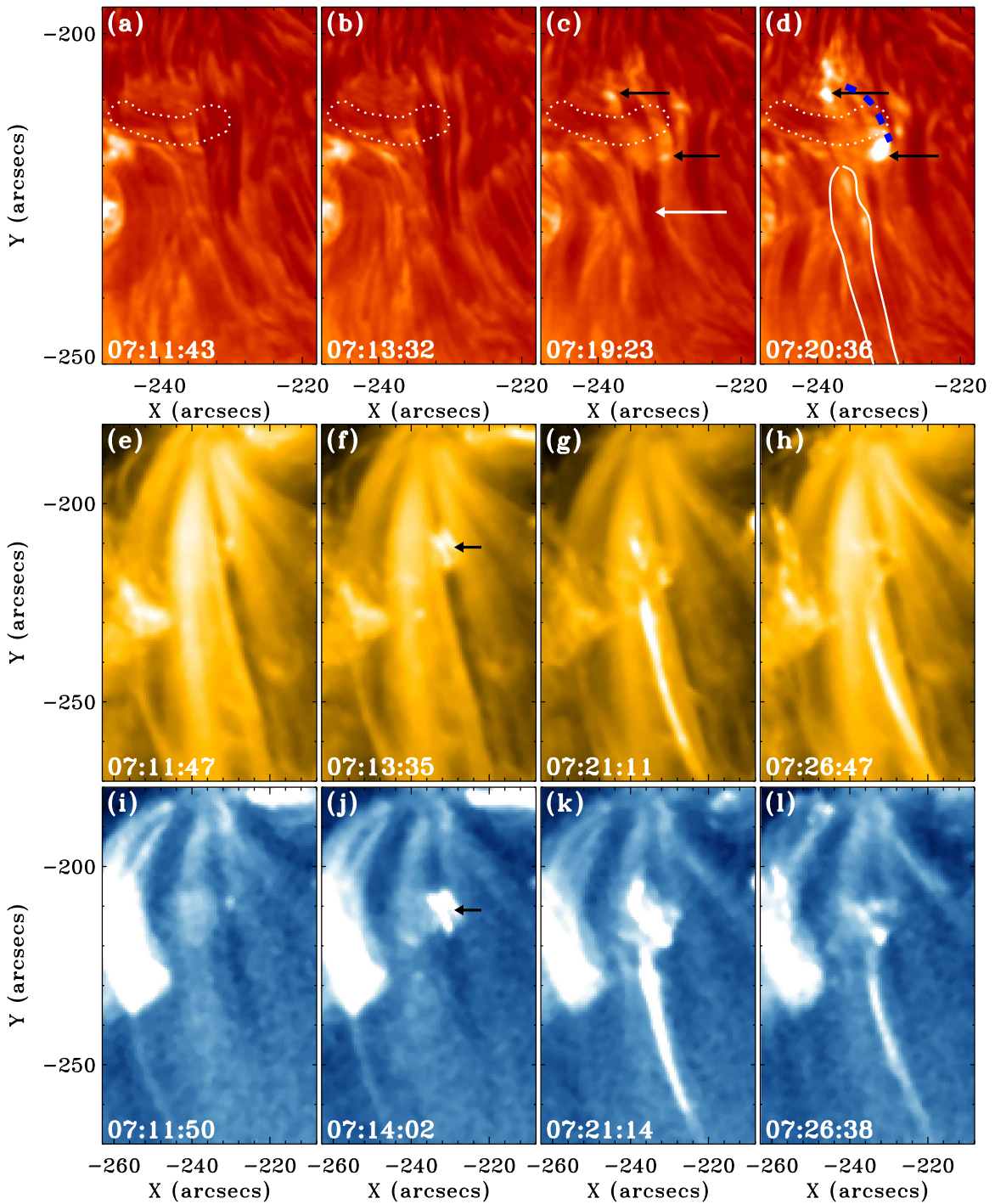


Figure 2. Evolution of the first ejection stage of the blowout jet. Panels (a)—(d): NVST $H\alpha$ -center images. Panels (e)—(h) and (i)—(l): AIA 171 and 335 Å images, respectively. The mini-filament is highlighted in the $H\alpha$ images with dotted contours. In panel (c), the two black arrows point to the pair of bright patches on either side of the mini-filament, while the white arrow points to the dark $H\alpha$ jet body. The arrows in panels (f) and (j) indicate the bright loop-like feature, whose position is overlaid in panel (d) as a blue dashed curve. The outline contour sketch of the coronal jet determined from the AIA 171 Å image at 07:21:11 UT is overlaid in panel (d). An animation is available in the online journal.

(An animation of this figure is available.)

blobs that move along the jet axis (see the green short arrows in panels (h) and (i) in Figure 3), which may show the magnetic reconnection process in the formation of the coronal blowout jet. Similar observations of plasma blob structures in coronal jets have been documented in a few studies (e.g., Ohya & Shibata 1998; Takasao et al. 2012; Kumar & Cho 2013; Zhang & Ji 2014b; Zhang et al. 2016), and very

recently, Ni et al. (2017) reproduced this physical process in their simulation.

The kinematics analysis of the blowout jet is presented in Figure 4 using time-distance diagrams made from NVST $H\alpha$, and AIA 304, 211, 131, and 335 Å observations along the jet axis as the dotted curve indicated in Figure 3(h), in which each time-distance diagram is obtained by composing the time sequence of

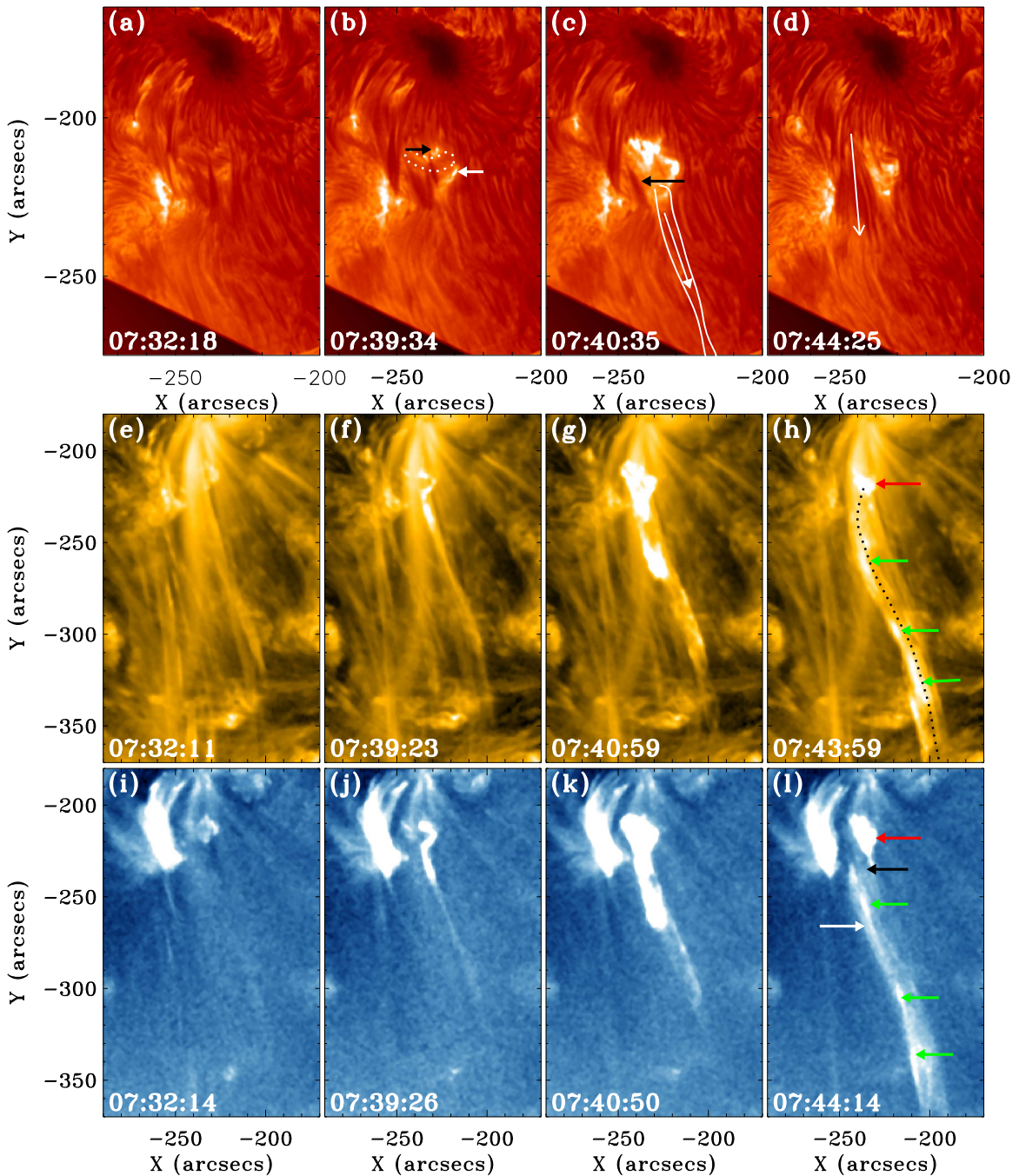


Figure 3. Evolution of the second ejection stage of the blowout jet. Panels (a)—(d): NVST $H\alpha$ -center images. Panels (e)—(h) and (i)—(l): AIA 171 and 335 Å images, respectively. The two arrows in panel (b) point to the bright patches on either side of the mini-filament, which is outlined by the white dotted contour. The arrow in panel (c) points to the erupting mini-filament, while the long white arrows in panels (d) and (d) indicate the direction of the $H\alpha$ jet. The white contour in panel (c) is the outline contour sketch of the coronal jet determined from the AIA 171 Å image at 07:39:23 UT. The dotted curve in panel (h) shows the path used to the obtain time-distance diagrams shown in Figure 4. The black and white arrows in panel (l) indicate the cool and hot components of the jet. The red arrows in panels (h) and (i) indicate the bright loop structure at the jet-base, and the green arrows point to the moving bright plasma blobs.

the intensity profiles along the jet axis. For each time-distance diagram, the abscissa and ordinate represent time and distance from the jet-base, respectively. The ejection speed of the jet can be obtained by measuring the slope of the inclined bright stripe that represents the ejecting jet. As shown in the figure, the two ejection stages of the blowout jet formed two bright stripes within about 40 minutes. The jet formed in the first stage has a relatively simple structure and an average speed of 340 km s^{-1} , while the jet formed in the second stage is more complicated and has an average speed of 300 km s^{-1} . It can be seen that the jet structure

in the second ejection stage in the AIA time-distance diagrams shows fine bright alternating dark stripes. This is caused by the ejecting plasma blobs along the jet axis rather than the cool (dark) and hot (bright) components as observed in the imaging observations. In the time-distance diagrams, each bright stripe represents a moving plasma blob. It is found that the moving speed of the blobs is in agreement with previous observational studies (Takasao et al. 2012; Kumar & Cho 2013; Zhang & Ji 2014b; Zhang et al. 2016). Here, the jet speeds are measured from the four AIA time-distance diagrams. The jets are hard to

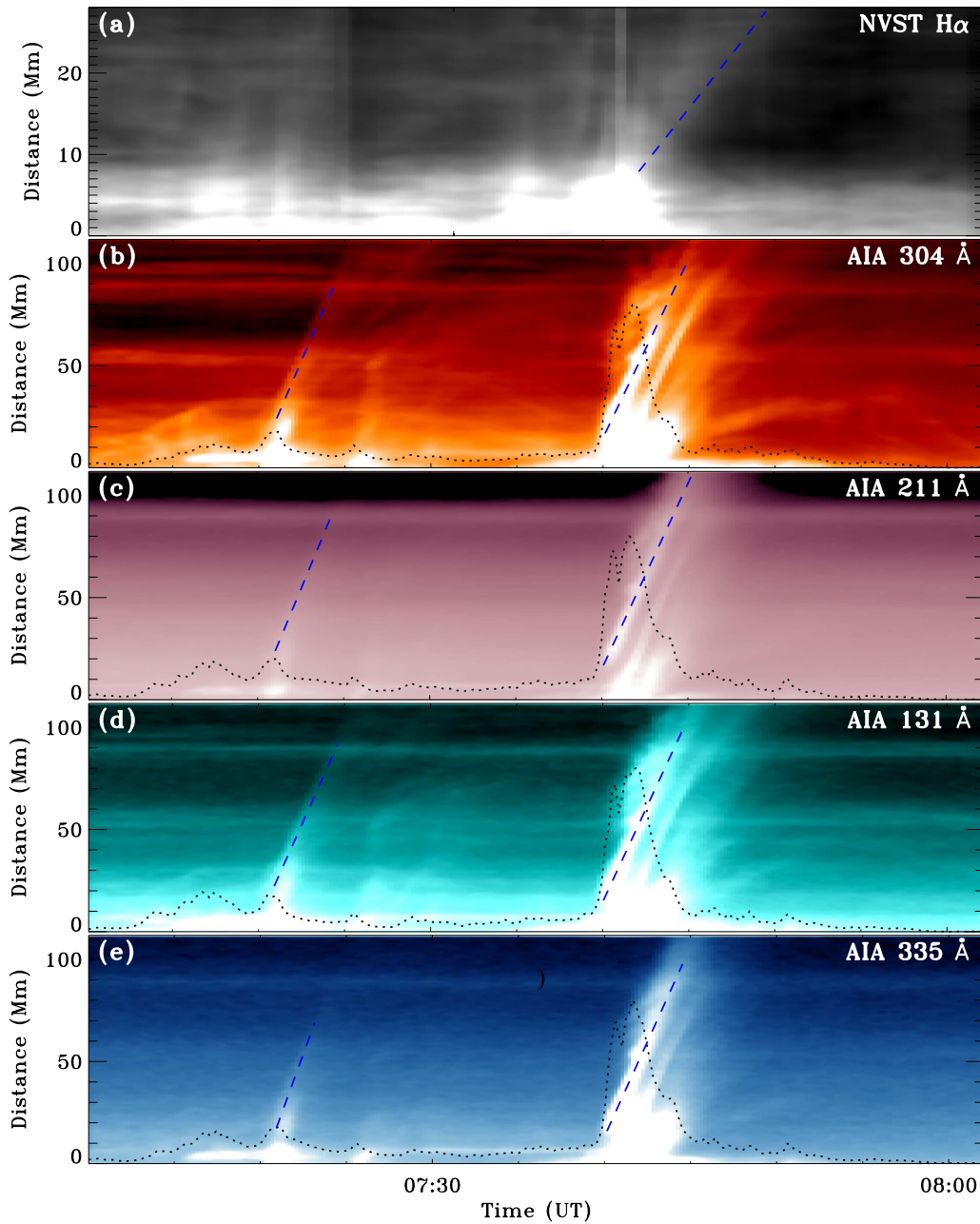


Figure 4. Time-distance diagrams show the kinematics of the ejection blowout jet. Panel (a): presents NVST $H\alpha$ observations, and panels (b)–(d) show AIA 304, 211, 131, and 335 Å base-difference images along the ejection direction, as indicated by the black dotted curve in Figure 3(h). The dotted lines are a linear fit to the paths of the jets, and the corresponding wavelengths are also plotted in the top right corner of each panel. The black dotted curve in panels (b)–(e) shows the normalized corresponding intensity light-curves of the source region of the eruption.

identify in the $H\alpha$ time-distance diagram (see Figure 4(a)). We trace the dark edge during the second stage of the jet to estimate the moving speed, which represents the top of the $H\alpha$ jet (see the dashed line in Figure 4(a)). It is obtained that the ejection speed is about 50 km s^{-1} , which is much slower than the speed obtained from AIA observations.

The evolution of the photospheric magnetic field in the eruption source region is displayed in Figure 5 using the HMI LOS magnetograms, in which the white and black patches represent the positive and negative magnetic polarities, respectively. In the meantime, the outline contour sketch of the mini-filament is overlaid in each panel to show its position in relation with the surrounding photospheric magnetic field. It can be seen that the mini-filament is located on the magnetic

polarity inversion line and the two ends are rooted in opposite polarities (P1 and N1). It is noted that a small southward-moving positive magnetic polarity (P) near the west end of the filament interacted with the negative polarity in which the western end of the filament was rooted in. When the small positive polarity moved, its area became smaller and smaller and eventually disappeared at about 07:35:49 UT (see the white arrow in the top row of Figure 5). This evolution process suggests that the small positive magnetic polarity was cancelled by the nearby negative magnetic field (N1). We further measured the positive and negative magnetic fluxes in the white box region shown in Figure 5(b), and the variation of the positive (red) and negative (blue) magnetic fluxes are plotted in Figure 5(e). It is found that the positive magnetic flux increases

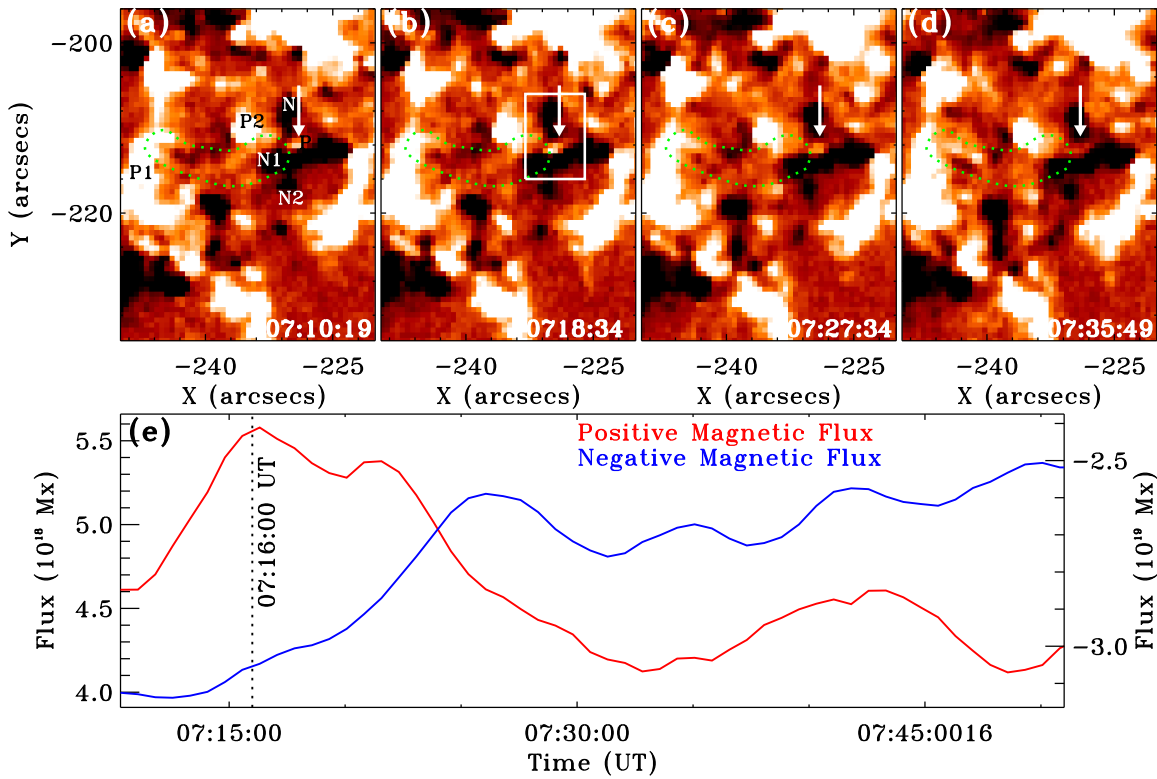


Figure 5. Detailed evolution of the magnetic field of the eruption source region. Panels (a)—(d): HMI LOS magnetograms. The green dotted curves overlaid on the magnetograms indicate the location of the mini-filament, and the vertical white arrow points to a small positive magnetic polarity. P, N, P1, N1, P2, and “N2” indicate the magnetic polarities involved in the present event. Panel (e): variations of the positive (red) and negative (blue) magnetic fluxes in the white box region, as shown in panel (b). The vertical dotted line in panel (e) indicates the start time of the magnetic cancellation.

quickly from 07:11:00 UT to 07:16:00 UT and then started a rapid decreasing phase. In the meantime, the negative magnetic flux decreased monotonously from 07:13:00 UT, but the decreasing speed obviously slowed down after 07:25:00 UT. The evolution process of the photospheric magnetic fluxes indicates that the magnetic cancellation was caused by the emerging and southward-moving small positive magnetic polarity. Taking the chromospheric and coronal eruption characteristics of the blowout jet into account, we propose that the initiation of the jet was caused by the emergence and cancellation of the small positive magnetic polarity at the western end of the mini-filament. The magnetic cancellation can first cause the disconnection of the western end of the mini-filament from the solar surface, and then the rising of the mini-filament and its overlying confining magnetic field. Eventually, the rising confining field of the mini-filament will reconnect with the overlying open magnetic field and thus results in the observed solar jet in the first ejection stage.

This blowout jet was also recorded by the metric radio spectrometer of YNAO, and the dynamic spectrum is shown in Figure 6. From the radio spectrum shown in Figure 6(a), one can identify some small radio bursts at around 07:16:00 UT and 07:40:00 UT (see the two white box regions in Figure 6(a)). The two time slots correspond well to the very beginning phases of the two ejection stages of the blowout jet. The close-up views of the two selected regions as shown by the two boxes in Figure 6(a) are plotted in Figures 6(b) and (c), respectively. It is clear that there are many radio type III bursts at around 07:16:12 UT and radio type III-like bursts at around 07:40:12 UT that have a negative frequency drift. Since type III bursts represent the signature of propagating beams of nonthermal

electrons in the solar atmosphere and are often associated with solar jets, they are thought to result from the magnetic reconnection between closed and open magnetic fields (Chifor et al. 2008; Nitta et al. 2008; Kumar & Cho 2013; Reid & Ratcliffe 2014; Innes et al. 2016; Hong et al. 2017). Therefore, the detection of radio type III bursts at the very beginning of the first stage of the jet indicates the start of the magnetic reconnection process between the overlying open magnetic field and the confining loops of the mini-filament. Since the drifting radio type III-like bursts have a negative frequency drift rate, they suggest that the emission sources are moving from low to high altitude during the second ejection stage of the jet. By measuring the observed frequency of the radio type III-like bursts and the density model proposed in Aschwanden & Benz (1995), one can derive the propagation speed of the emission source (e.g., Gao et al. 2014b, 2016). Here, it is estimated that the upward-moving speed of the radio emission source is about 30 Mm^{-1} , which is about 100 times the ejection speed of the plasma blobs. With the wavelet analysis technique (Torrence & Compo 1998) that has been applied to analyze various periods (e.g., Shen & Liu 2012; Shen et al. 2013, 2015; Deng et al. 2012, 2013; Xie et al. 2012; Li et al. 2015, 2017), it is obtained that the period of the radio type III-like bursts and the plasma blobs are about 4 and 90 seconds, respectively. Although the speeds and periods of the radio type III-like bursts show significant difference with those of the plasma blobs, the two phenomena are tightly related to the magnetic reconnection process that produces the observed jet.

To further analyze the physical property of the observed plasma blobs, the high-temperature wavelength filters of AIA

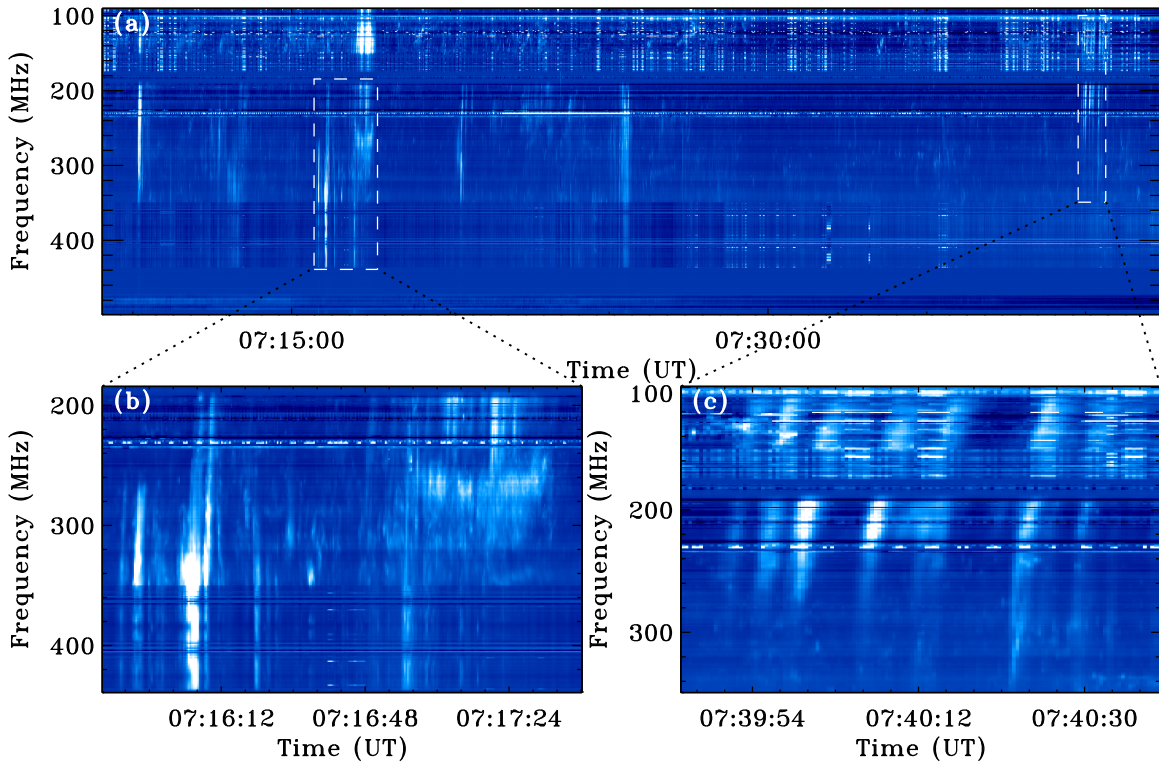


Figure 6. Dynamic spectrum observed by the YNAO spectrometer. Panel (a): right- and left-polarization spectrum maps from 07:09:02 UT to 07:42:22 UT in the frequency range of 90–499 MHz. Panels (b) and (c): close-up views of the same two box regions as are shown in the top panel, and their time intervals are 120 and 52 seconds, respectively. The vertical bright ridges are the type III radio bursts. Note that the frequency ranges of panels (b) and (c) are 184–439 and 99–349 MHz, respectively.

94 and 131 Å are shown in Figures 7(a) and (b), respectively. The plasma blobs can be identified as bright patches along the jet axis, as indicated by the arrows in Figure 7(b). The peak temperature and emission measure of the plasma blobs are analyzed with the differential emission measure (DEM) software available in the Solar SoftWare (SSW) package (Aschwanden et al. 2013). The code uses the six coronal temperature wavelength filters of AIA (i.e., 94, 131, 171, 193, 211, and 335 Å), and the parameters of the peak emission measure (EM_p), the peak temperature (T_p), and the temperature width sigma (σ_T) can be obtained by fitting the DEM distribution function (Gaussian distribution) in each pixel. The emission measure and temperature maps of the jet are shown in Figures 7(c) and (d), respectively. It can be seen that the temperature of the eruption source region and positions of the plasma blobs along the jet are up to ~ 6 MK. For comparison of the physical parameters of the plasma blobs with previous observations (Kumar & Cho 2013), we also calculate the total emission measure (TEM) in the selected regions using the formula $\int DEM(T)dT$. Using this value, we can estimate the densities (n_e) of the plasma blobs with the relation $n_e = \sqrt{\frac{EM}{L}}$ by assuming that the depth of the structure along the LOS is equal to its width (Cheng et al. 2012). Here, EM and L are the emission measure and the width of the blobs, and we assume the filling factor to be 1, as in Kumar & Cho (2013). Table 1 shows all the calculated parameters of the plasma blobs. It can be seen that the peak temperature of the plasma blobs varies from ~ 1.4 to 1.5 MK, which is slightly lower than the value (~ 1.6 to 3.4 MK) presented in Kumar & Cho (2013) and much lower than those (~ 10 MK) derived from X-ray observations (e.g., Ohyama & Shibata 1998; Nishizuka

et al. 2010). The average density varies from 1.61×10^{10} to $2.89 \times 10^{10} \text{ cm}^{-3}$. It is found that the densities of the plasma blobs decrease with increasing distance from the eruption source region of the jet, but their temperatures are almost the same. The decreasing density of the plasma blobs may suggest that the dissipation process is active during their propagation.

4. Interpretation

In order to better understand the physics during the initiation and evolution of the blowout jet, a simple sketch is plotted in Figure 8 to illustrate the detailed evolution process. It should be pointed out that only some representative magnetic field lines are plotted in the figure. Figure 8(a) shows the initial magnetic topology of the eruption source region, and the arrow on each curve indicates the direction of the magnetic field. Positive (P, P1, and P2) and negative (N, N1, and N2) polarities are plotted in analogy to the HMI LOS magnetogram as shown in Figure 5(a). According to the observational results, the mini-filament connects magnetic polarities of P1 and N1 (black thick curve), and it is confined by a group of closed coronal loops that connects magnetic polarities of P2 and N2 (yellow). In addition, above the confining field of the mini-filament lies another group of open coronal loops that is rooted in negative polarity N. In this magnetic topology, it is clear that a current sheet can be formed between the overlying open loops and the confining loop of the mini-filament if the magnetic system is subject to some external or internal disturbances.

The blowout jet is initiated from the emergence of the small positive-polarity P nearby the negative end of the mini-filament (N1), which approaches N1 and causes the magnetic cancellation between the polarities of P and N1. This will cause the

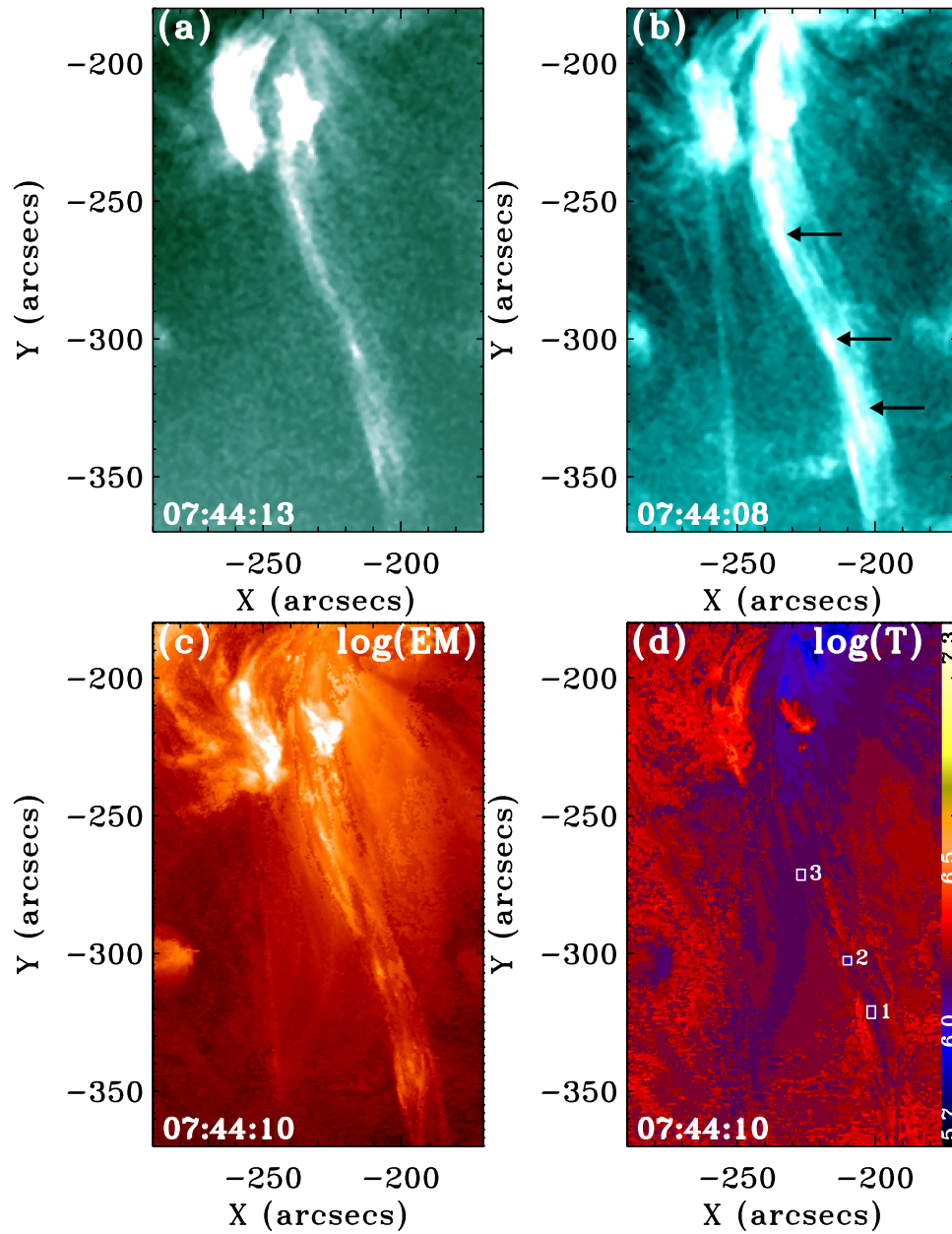


Figure 7. DEM analysis of the plasma blobs at 07:44:10 UT. Panels (a) and (b): AIA 94 and 131 Å images, respectively. The moving plasma blobs are indicated with the three black arrows in panel (b). Panels (c) and (d): peak emission measure ($\text{cm}^{-5} \text{K}^{-1}$) and temperature (MK) maps, respectively. The color bar on the right of panel (d) indicates the temperature variation range of the temperature map.

disconnection of the mini-filament magnetic field from N1 and further lead to the rise of the mini-filament as well as the overlying confining coronal loops (Figure 8(b)). Owing to the rising confining loops, a current sheet can be formed between the closed confining loops and the overlying open loops. The continued rise of the confining loops will trigger magnetic reconnection in the current sheet, which not only produces the first ejection stage of the blowout jet, but also the radio type III bursts that show the upward-moving beams of nonthermal electrons along the reconnected open magnetic loops (see Figure 8(c)). In the meantime, bright patches can be expected at the polarities of N2, P2, and N because the cool chromosphere material is heated by the downward-moving nonthermal particles along the reconnected field lines (red). In our observation, we do observe bright patches at N2 and P2, and the bright loop structure connecting P2 and N2 can also be

explained as the heated confining loops due the magnetic reconnection. In our observation, the brightening patches and the radio type III bursts provide evidence for the occurrence of magnetic reconnection between the closed and open magnetic fields.

Another consequence of the magnetic reconnection between the closed and open field is the successive removal of the magnetic confinement that prevents the mini-filament from erupting. This will further accelerate the rise and the violent eruption of the mini-filament. As shown in Figure 8(d), the cool erupting filament material merges with the nearby hot jet from the reconnection region and therefore forms the cool and hot components of the blowout jet. As in the first stage, the pair of bright patches on either side of the mini-filament suggests the occurrence of magnetic reconnection between the rising closed confining loops and the overlying open loops. In addition, the

Table 1
Temperature, Density, and Other Parameters of the Observed Plasma Blobs

Date/Time (UT)	Boxes	$\log(T_p)$ (MK)	$\log(EM_p)$ ($\text{cm}^{-5} \text{K}^{-1}$)	σ_T	TEM cm^{-5}	L (arcsec)	n_e cm^{-3}
04/16/2014 07:44:10	1	6.18	20.92	0.27	6.06×10^{28}	3.2	1.61×10^{10}
	2	6.16	21.05	0.33	1.88×10^{29}	5.5	2.16×10^{10}
	3	6.18	21.21	0.16	3.52×10^{29}	5.8	2.89×10^{10}

observed plasma blobs are possibly due to the tearing instability during the turbulent magnetic reconnection, while the periodic radio type III-like bursts during this stage are possibly caused by some nonlinear acceleration process of electrons during the magnetic reconnection.

5. Conclusions and Discussions

Using high temporal and high spatial resolution observations taken by NVST, *SDO*, and the metric spectrometer of YNAO, we present the multiwavelengths observation of a miniature solar blowout jet that occurred at the southern periphery of the preceding sunspot of NOAA active region AR12035. The blowout jet was associated with the eruption of a mini-filament that resides in the magnetic polarity inversion region and has a length of about 13 Mm. The ejection of the blowout jet can be divided into two stages. The first stage includes the initiation and ejection of a small jet, while the second stage is associated with the eruption of the mini-filament and the generation of the jet's cool and hot fine structures. It is measured that the ejection speeds of the jets during the first and the second stage are about 340 and 300 km s^{-1} , respectively. During the ejection, magnetic reconnection characteristics such as the bright patches on either side of the mini-filament, hot plasma blobs along the jet body, and periodic metric radio type III bursts around the beginning of the two ejection stages are observed. The appearance and evolution characteristics of these features show the detailed magnetic reconnection process between the closed confining loops of the mini-filament and the overlying open loops.

It is found that the initiation of the blowout jet was caused by the emergence of a small positive magnetic polarity, which was cancelled by the negative magnetic field at the western end of the mini-filament. The magnetic cancellation directly resulted in the rise of the mini-filament and its confining loops, which further caused the magnetic reconnection between the closed confining loops of the mini-filament and the overlying open loops. The heated plasma flow that was accelerated in the magnetic reconnection region formed the observed bright jet structure in the first stage. The observed bright patches on either side of the filament are possibly caused by the heating of the cool chromosphere material at the two ends of the closed reconnected loops by the downward-moving nonthermal particles from the reconnection region. In the meantime, the reconnection also accelerates electrons that move along the open reconnected loops, which causes the observed metric radio type III bursts. During the first ejection stage, both dark (cool) $H\alpha$ and bright (hot) coronal jets are observed along the same trajectory, and they showed an obvious eastward whip-like motion. The appearance time of the cool $H\alpha$ jet was earlier than the appearance of its hot coronal counterpart. This suggests that the height of the magnetic reconnection was possibly lower in the chromosphere, which first drives the $H\alpha$ jet and then the coronal counterpart. Another possibility is that

the formation of the hot coronal jet is due to the heating of the cool $H\alpha$ counterpart in the chromosphere, since we do find that the cool $H\alpha$ jet became brighter than before at around the appearance of the hot coronal counterpart. Chae et al. (1999) also reported observations of cospatial bright $H\alpha$ jets and hot coronal jets, and they proposed that the $H\alpha$ jets and the corresponding coronal jets are different types of plasma flows along different field lines that are dynamically connected to each other.

The second ejection stage of the blowout jet underwent a blowout process of the jet-base involving the mini-filament. The eruption of the mini-filament is due to two possible reasons: one reason is magnetic cancellation at the western end of the mini-filament, which directly results in the disconnection of the mini-filament from the solar surface; The other reason is the successive removal of the magnetic confinement of the overlying loops since the magnetic reconnection during the first ejection stage. We observed many eruption characteristics during the second ejection stage of the blowout jet, including the eastward whip-like motion of the jet body, two bright patches on either side of the filament connected by a bright loop, periodic metric radio type III-like bursts with a period of 4 seconds at the beginning of the second ejection, and plasma blobs with a period of about 90 seconds along the jet body. We propose that all these observed eruption features are caused by the magnetic reconnection between the rising confining loops of the mini-filament and the overlying open loops, and the periodicity of the metric radio type III-like bursts and plasma blobs together show the detailed nonlinear process in the magnetic reconnection. With the DEM, it is estimated that the temperature of the observed plasma blobs varies from ~ 1.4 to 1.5 MK, which is slightly lower than the value presented in Kumar & Cho (2013) and much lower than the values derived from X-ray observations (e.g., Ohyama & Shibata 1998; Nishizuka et al. 2010). The estimated average density ranges from 1.61×10^{10} to $2.89 \times 10^{10} \text{ cm}^{-3}$, which shows a decreasing trend with increasing distance from the eruption source region, but the temperature of the blobs at different distances is almost the same. This may suggest that the dissipation process is active during the propagation of the blobs.

It is interesting that the erupting cool filament was adjacent to the previously existing bright jet body and therefore formed the observed cool (dark) and hot (bright) components of the blowout jet. It is measured that the appearance of the cool component delays the hot component by about five minutes. Here, the formation mechanism of the cool and hot components of the blowout jet is consistent with the observations reported by Shen et al. (2012), but different to many other studies (e.g., Schmieder et al. 1994; Alexander & Fletcher 1999; Jiang et al. 2007; Nishizuka et al. 2008; Yokoyama & Shibata 1995; Lee et al. 2013). However, the temporal and spatial relationship between the two components is consistent with previous observational studies (e.g., Alexander & Fletcher 1999; Jiang

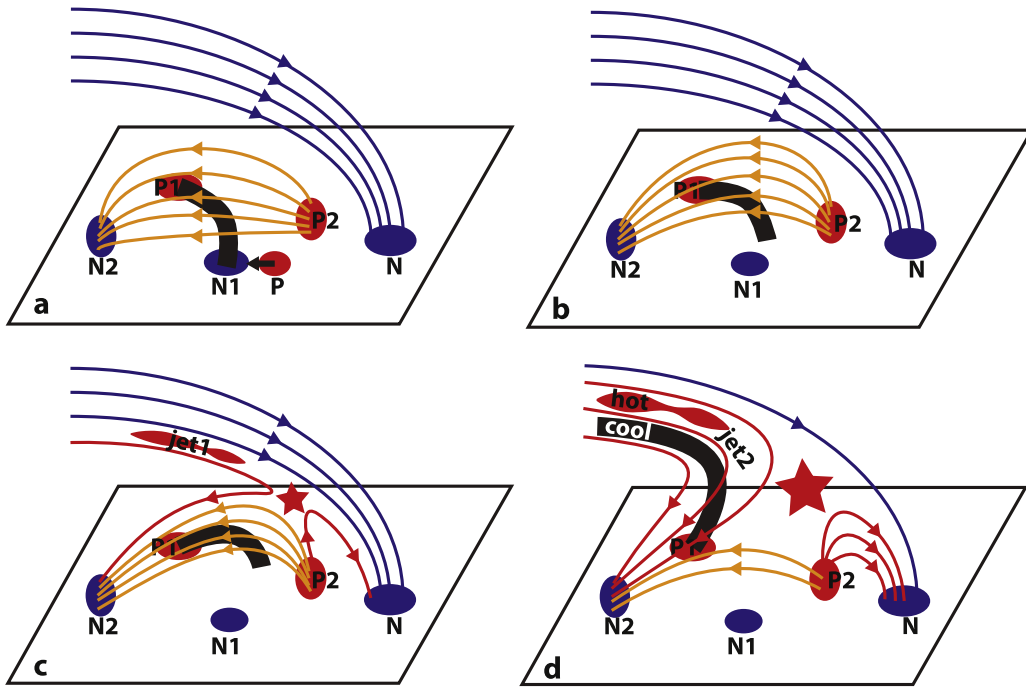


Figure 8. Cartoon in analogy with the observation to illustrate the eruption process of the blowout jet. Panel (a): topology of the magnetic field before the jet. Labels P, P1, and P2 represent the positive magnetic polarities, while N, N1, and N2 represent the negative magnetic polarities. The mini-filament connects P1 and N1 and is confined by a closed-loop system connecting P2 and N2, and another open-loop system rooted in N on the right. The black arrow indicates the moving direction of P. Panel (b): cancellation between P and N1 and the rise of the mini-filament. Panel (c): magnetic reconnection between the closed and open loops and the formation of the jet during the first ejection stage. Panel (d): eruption of the mini-filament and the formation of the cool and hot components of the jet during the second ejection stage. The red lines show the reconnected magnetic field lines, and the red five-pointed star indicates the reconnection position. The red sausage features in panels (c) and (d) indicate the hot plasma flow (jet) generated by the magnetic reconnection.

et al. 2007). It should be emphasized that there are two types of cool and hot components for solar jets. The first type is that the two components are observed in cool ($H\alpha$) and hot (EUV or X-ray) lines, respectively. The other type is that the cool and the hot components are both observed in hot coronal observations. In the present case, the cool and hot jets observed in the first ejection stage belong to the first case, while the cool and hot components observed in the second ejection stage belong to the second case.

Based on the observational results, a cartoon is proposed to interpret the ejection of the blowout jet. In our explanation, the cool jet component observed in the second ejection stage directly results from the eruption of the mini-filament at the jet-base, while the hot component is the outward-moving heated plasma flow that is generated in the magnetic reconnection. This interpretation is consistent with our previous observational result (Shen et al. 2012). The delayed appearance of the cool component is a natural consequence of the blowout jets in Shen et al. (2012) and the present event, because in both cases, the start time of the mini-filament eruption is always after the magnetic reconnection that generates the hot plasma flow. The explanations of the formation and delay appearance of the cool component in the blowout jet are different, with various interpretations proposed in previous observational and simulation studies. For example, many authors have proposed that the cool component is formed by the cooling of the preceding hot component (e.g., Schmieder et al. 1994; Alexander & Fletcher 1999; Jiang et al. 2007) or caused by reconnection of emerging flux in the transition region or upper chromosphere (Lee et al. 2013). In addition, simulation works have suggested that the cool component is formed by chromosphere cool

plasmas that are carried up with expanding loops and accelerated by the tension force of disconnected field lines (Yokoyama & Shibata 1995; Chae et al. 1999), and Nishizuka et al. (2008) proposed that the delay of the cool component is due to the different Alfvén velocities in the cool (high-density) and hot (low-density) plasma rather than the cooling effect. To better understand the formation mechanism of the cool component in solar jets, simulation works and more observational studies based on high temporal and high spatial multiwavelength observations are needed in the future.

We thank the observations provided by NVST, *SDO*, and the metric spectrometer of YNAO. We also thank the anonymous referee for their suggestions and comments that largely improved the quality of the present paper, and Dr. G. Gao in the Yunnan observatories of the Chinese Academy of Sciences for her help with the radio data analysis and explanations. This work is supported by the Natural Science Foundation of China (11403097, 11633008, 11773068), the Yunnan Science Foundation (2015FB191, 2017FB006), the Specialized Research Fund for State Key Laboratories, the Open Research Program of the Key Laboratory of Solar Activity of Chinese Academy of Sciences (KLSA201601), the Youth Innovation Promotion Association (2014047) of Chinese Academy of Sciences.

ORCID iDs

Yuandeng Shen <https://orcid.org/0000-0001-9493-4418>
 Ying D. Liu <https://orcid.org/0000-0002-3483-5909>
 Zhining Qu <https://orcid.org/0000-0001-8318-8747>
 Zhanjun Tian <https://orcid.org/0000-0002-7418-168X>

References

- Aschwanden, M. J., & Benz, A. O. 1995, *ApJ*, **438**, 997
- Aschwanden, M. J., Boerner, P., Schrijver, C. J., & Malanushenko, A. 2013, *SoPh*, **283**, 5
- Adams, M., Sterling, A. C., Moore, R. L., & Gary, G. A. 2014, *ApJ*, **783**, 11
- Alexander, D., & Fletcher, L. 1999, *SoPh*, **190**, 167
- Archontis, V., & Hood, A. W. 2013, *ApJL*, **769**, L21
- Brooks, D. H., Kurokawa, H., & Berger, T. E. 2007, *ApJ*, **656**, 1197
- Canfield, R. C., Reardon, K. P., & Leka, K. D. 1996, *ApJ*, **464**, 1016
- Chae, J., Qiu, J., Wang, H., & Goode, P. R. 1999, *ApJL*, **513**, L75
- Cheng, X., Zhang, J., Saar, S. H., & Ding, M. D. 2012, *ApJ*, **761**, 62
- Chifor, C., Isobe, H., Mason, H. E., et al. 2008, *A&A*, **491**, 279
- Curdt, W., & Tian, H. 2011, *A&A*, **532**, 9
- Curdt, W., Tian, H., & Kamio, S. 2012, *SoPh*, **280**, 417
- Chen, H. D., Jiang, Y. C., & Ma, S. L. 2008, *A&A*, **478**, 907
- Chen, H., Jiang, Y., & Ma, S. 2009, *SoPh*, **255**, 79
- Chen, H., Zhang, J., Cheng, X., et al. 2014, *ApJL*, **797**, 15
- Chen, H.-D., Zhang, J., & Ma, S.-L. 2012, *RAA*, **12**, 573
- Chen, H., Zhang, J., Li, L., & Ma, S. 2016, *ApJL*, **818**, 27
- Chen, J., Su, J., Yin, Z., et al. 2015, *ApJ*, **815**, 71
- Chen, J., Su, J., Deng, Y., & Priest, E. R. 2017, *ApJ*, **840**, 54
- Deng, L.-H., Qu, Z.-Q., Yan, X.-L., & Wang, K.-R. 2013, *RAA*, **13**, 104
- Deng, L. H., Qu, Z. Q., Yan, X. L., Liu, T., & Wang, K. R. 2012, *JApA*, **33**, 221
- Filippov, B., Srivastava, A. K., Dwivedi, B. N., et al. 2015, *MNRAS*, **451**, 1117
- Gao, G., Wang, M., Dong, L., Wu, N., & Lin, J. 2014a, *NewA*, **30**, 68
- Gao, G.-N., Wang, M., Lin, J., et al. 2014b, *RAA*, **14**, 843
- Gao, G., Wang, M., Wu, N., et al. 2016, *SoPh*, **291**, 3369
- Guo, Y., Démoulin, P., Schmieder, B., et al. 2013, *A&A*, **555**, A19
- He, J.-S., Marsch, E., Curdt, W., et al. 2010, *A&A*, **519**, A49
- Hong, J., Jiang, Y., Zheng, R., et al. 2011, *ApJL*, **738**, 20
- Hong, J., Jiang, Y., Yang, J., et al. 2013, *RAA*, **13**, 253
- Hong, J., Jiang, Y., Yang, J., et al. 2014, *ApJ*, **796**, 73
- Hong, J., Jiang, Y., Yang, J., et al. 2016, *ApJ*, **830**, 60
- Hong, J., Jiang, Y., Yang, J., Li, H., & Xu, Z. 2017, *ApJ*, **835**, 35
- Innes, D. E., Bućík, R., Guo, L.-J., & Nitta, N. 2016, *AN*, **337**, 1024
- Innes, D. E., Inhester, B., Axford, W. I., & Wilhelm, K. 1997, *Natur*, **386**, 811
- Jiang, Y., Bi, Y., Yang, J., et al. 2013, *ApJ*, **775**, 132
- Jiang, Y., Shen, Y., Bi, Y., Yang, J., & Wang, J. 2008, *ApJ*, **677**, 699
- Jiang, Y. C., Chen, H. D., Li, K. J., Shen, Y. D., & Yang, L. H. 2007, *A&A*, **469**, 331
- Joshi, R., Schmieder, B., Chandra, R., et al. 2017, *SoPh*, **292**, 152
- Kayshap, P., Srivastava, A. K., & Murawski, K. 2013, *ApJ*, **763**, 24
- Kumar, P., & Cho, K.-S. 2013, *A&A*, **557**, A115
- Lee, E. J., Archontis, V., & Hood, A. W. 2015, *ApJ*, **799**, 79
- Lee, K.-S., Innes, D. E., Moon, Y.-J., et al. 2013, *ApJ*, **766**, 1
- Lemen, J. R., Tittle, A. M., Akin, D. J., et al. 2012, *SoPh*, **275**, 17
- Li, D., Ning, Z., & Su, Y. 2016, *Ap&SS*, **361**, 301
- Li, D., Ning, Z. J., & Zhang, Q. M. 2015, *ApJ*, **807**, 72
- Li, D., Ning, Z., Huang, Y., et al. 2017, *ApJ*, **849**, 113
- Li, H., Jiang, Y., Yang, J., et al. 2017a, *ApJ*, **836**, 235
- Li, H., Jiang, Y., Yang, J., et al. 2017b, *ApJL*, **842**, L20
- Li, H. D., Jiang, Y. C., Yang, J. Y., Bi, Y., & Liang, H. F. 2015, *Ap&SS*, **359**, 44
- Li, L. P., Zhang, J., Li, T., Yang, S. H., & Zhang, Y. Z. 2012, *A&A*, **539**, A7
- Li, X., Yang, S., Chen, H., Li, T., & Zhang, J. 2015, *ApJL*, **814**, L13
- Lim, E.-K., Yurchyshyn, V., Park, S.-H., et al. 2016, *ApJ*, **817**, 39
- Liu, J., Wang, Y., Shen, C., et al. 2015, *ApJL*, **813**, 115
- Liu, W., Berger, T. E., Tittle, A. M., & Tarbell, T. D. 2009, *ApJL*, **735**, L18
- Liu, Y. 2008, *SoPh*, **249**, 75
- Liu, Y., & Kurokawa, H. 2004, *ApJ*, **610**, 1136
- Liu, Y., Su, J. T., Morimoto, T., Kurokawa, H., & Shibata, K. 2005, *ApJ*, **628**, 1056
- Liu, Z., Xu, J., Gu, B.-Z., et al. 2014, *RAA*, **14**, 705
- Moore, R. L., Cirtain, J. W., Sterling, A. C., & Falconer, D. A. 2010, *ApJ*, **720**, 757
- Moore, R. L., Sterling, A. C., & Falconer, D. A. 2015, *ApJ*, **806**, 11
- Moore, R. L., Sterling, A. C., Hudson, H. S., & Lemen, J. R. 2001, *ApJ*, **552**, 833
- Mulay, S. M., Zanna, G. D., & Mason, H. 2017, *A&A*, **606**, A4
- Ni, L., Kliem, B., Lin, J., & Wu, N. 2015, *ApJ*, **799**, 79
- Ni, L., Zhang, Q., Murphy, N. A., & Lin, J. 2017, *ApJ*, **841**, 27
- Nishizuka, N., Shimizu, M., Nakamura, T., et al. 2008, *ApJ*, **683**, 83
- Nishizuka, N., Takasaki, H., Asai, A., & Shibata, K. 2010, *ApJ*, **711**, 1062
- Nisticò, G., Bothmer, V., Patsourakos, S., & Zimbardo, G. 2009, *SoPh*, **259**, 87
- Nitta, N. V., Mason, G. M., Wiedenbeck, M. E., et al. 2008, *ApJL*, **675**, L125
- Ohyama, M., & Shibata, K. 1998, *ApJ*, **499**, 934
- Panesar, N. K., Sterling, A. C., Moore, R. L., & Chakrapani, P. 2016, *ApJL*, **832**, 7
- Pariat, E., Antiochos, S. K., & DeVore, C. R. 2009, *ApJ*, **691**, 61
- Pariat, E., Antiochos, S. K., & DeVore, C. R. 2010, *ApJ*, **714**, 1762
- Pariat, E., Dalmasse, K., DeVore, C. R., Antiochos, S. K., & Karpen, J. T. 2015, *A&A*, **573**, 130
- Pariat, E., Dalmasse, K., DeVore, C. R., Antiochos, S. K., & Karpen, J. T. 2016, *A&A*, **596**, 36
- Pesnell, W. D., Thompson, B. J., & Chamberlin, P. C. 2012, *SoPh*, **275**, 3
- Pucci, S., Poletto, G., Sterling, A. C., & Romoli, M. 2013, *ApJ*, **776**, 16
- Raouafi, N. E., Patsourakos, S., Pariat, E., et al. 2016, *SSRv*, **201**, 1
- Reid, H. A. S., & Ratcliffe, H. 2014, *RAA*, **14**, 773
- Schmieder, B., Golub, L., & Antiochos, S. K. 1994, *ApJ*, **425**, 326
- Schmieder, B., Guo, Y., Moreno-Insertis, F., et al. 2013, *A&A*, **559**, 1
- Schou, J., Borrero, J. M., Norton, A. A., et al. 2012, *SoPh*, **275**, 229
- Shen, Y., Ichimoto, K., Ishii, T. T., et al. 2014, *ApJ*, **786**, 151
- Shen, Y., Liu, Y., Su, J., & Ibrahim, A. 2011, *ApJL*, **735**, 43
- Shen, Y., Liu, Y., Su, J., & Deng, Y. 2012, *ApJ*, **745**, 164
- Shen, Y., Liu, Y., Liu, Y. D., et al. 2015, *ApJL*, **814**, L17
- Shen, Y.-D., Liu, Y., Su, J.-T., et al. 2013, *SoPh*, **288**, 585
- Shen, Y., & Liu, Y. 2012, *ApJ*, **753**, 53
- Shibata, K., & Uchida, Y. 1986, *SoPh*, **103**, 299
- Shibata, K., Nakamura, T., Matsumoto, T., et al. 2007, *Sci*, **318**, 1591
- Shibata, K., Nitta, N., Matsumoto, R., et al. 1994a, in Proc. Intl. Symp. on the *Yohkoh* Scientific Results, X-Ray Solar Physics from *Yohkoh*, ed. Y. Uchida et al. (Tokyo: Universal Academy Press), 29
- Shibata, K., Nitta, N., Strong, K. T., et al. 1994b, *ApJL*, **431**, 51
- Sterling, A. C., Moore, R. L., Falconer, D. A., & Adams, M. 2015, *Natur*, **523**, 437
- Sterling, A. C., Moore, R. L., Falconer, D. A., et al. 2016, *ApJ*, **821**, 100
- Su, W., Cheng, X., Ding, M. D., Chen, P. F., & Sun, J. Q. 2015, *ApJ*, **804**, 88
- Szente, J., Toth, G., Manchester, W. B., et al. 2017, *ApJ*, **834**, 123
- Takasao, S., Asai, A., Isobe, H., & Shibata, K. 2012, *ApJL*, **745**, L6
- Tian, H., DeLuca, E. E., Cranmer, S. R., et al. 2014, *Sci*, **346**, 315
- Tian, Z., Liu, Y., Shen, Y., et al. 2017, *ApJ*, **845**, 94
- Torrence, C., & Compo, G. P. 1998, *BAMS*, **79**, 61
- Wang, J., Li, W., Denker, C., et al. 2000, *ApJ*, **530**, 1071
- Wang, R., Liu, Y. D., Zimovets, I., et al. 2016, *ApJL*, **827**, 12
- Wang, Y.-M., Sheeley, N. R., Jr., Socker, D. G., et al. 1998, *ApJ*, **508**, 899
- Wyper, P. F., DeVore, C. R., Karpen, J. T., & Lynch, B. J. 2016, *ApJ*, **827**, 4
- Wyper, P. F., & DeVore, C. R. 2016, *ApJ*, **820**, 77
- Wyper, P. F., Antiochos, S. K., & DeVore, R. 2017, *Natur*, **544**, 452
- Xiang, Y.-Y., Liu, Z., & Jin, Z.-Y. 2016, *ApJ*, **830**, 60
- Xie, J.-L., Shi, X.-J., & Xu, J.-C. 2012, *RAA*, **12**, 187
- Xue, Z., Yan, X., Yang, L., Wang, J., & Zhao, L. 2017, *ApJL*, **840**, 23
- Yan, X. L., Xue, Z. K., Liu, J. H., Kong, D. F., & Xu, C. L. 2014, *ApJ*, **797**, 52
- Yan, X. L., Xue, Z. K., Pan, G. M., et al. 2015, *ApJS*, **219**, 17
- Yang, B., Jiang, Y., Yang, J., Yu, S., & Xu, Z. 2016, *ApJ*, **816**, 41
- Yang, J., Jiang, Y., Yang, B., et al. 2012b, *NewA*, **17**, 732
- Yang, J.-Y., Jiang, Y.-C., Yang, D., et al. 2012a, *RAA*, **12**, 300
- Yang, J.-Y., Jiang, Y. C., Yang, B., Hong, J., & Xu, Z. 2016, *RAA*, **16**, 3
- Yang, L.-H., Jiang, Y.-C., Yang, J.-Y., et al. 2011, *RAA*, **11**, 1229
- Young, P. R., & Muglach, K. 2014, *PASJ*, **66**, 12
- Yokoyama, T., & Shibata, K. 1995, *Natur*, **375**, 42
- Zhang, J., Wang, J., & Liu, Y. 2000, *A&A*, **361**, 759
- Zhang, Q. M., & Ji, H. S. 2014a, *A&A*, **561**, 134
- Zhang, Q. M., & Ji, H. S. 2014b, *A&A*, **567**, 11
- Zhang, Q. M., Li, D., Ning, Z. J., et al. 2016, *SoPh*, **291**, 859
- Zhang, Y., & Zhang, J. 2017, *ApJ*, **834**, 79
- Zhu, X., Wang, H., Cheng, X., & Huang, C. 2017, *ApJL*, **944**, L20
- Zheng, R., Jiang, Y., Yang, J., et al. 2012, *ApJ*, **747**, 67
- Zheng, R., Jiang, Y., Yang, J., et al. 2013, *ApJ*, **764**, 70
- Zheng, R., Chen, Y., Du, G., & Li, C. 2016, *ApJL*, **819**, L18